

Near Infrared Spectroscopy of the Ultracompact HII Region G45.12+0.13

S.L. Lumsden¹ and P.J. Puxley²

¹ Anglo-Australian Observatory, PO Box 296, Epping, NSW 2121, Australia – sll@aaoepp.aao.gov.au

² Royal Observatory Edinburgh, Blackford Hill, Edinburgh, EH9 3HJ, UK – pjp@roe.ac.uk

10 June 2021

ABSTRACT

We present complete, low resolution *IJHK* spectroscopy of the ultracompact HII region, G45.12+0.13. From the observed HI line strengths, we derive a near infrared extinction law that is slightly steeper than the average. After correction with this extinction law, we find good agreement between the observed line ratios of HeI, Fe⁺, Fe²⁺, S⁺ and S⁺⁺ and the available atomic data. Our data show that the density within the core of G45.12+0.13 must be at least 10⁴cm^{−3}. This is consistent with the known radio structure of the HII region and in considerable disagreement with previous work using mid and far infrared lines. There must also be considerable opacity in the HeI 2³P–2³S transition, and we show how the observed strengths of the other HeI lines are consistent with this. From modelling the photoionisation structure, we find good agreement with most of the observed data if the hottest star present has $T_{eff} \leq 42000\text{K}$. Consideration of the helium ionisation state places a lower limit on this value so that we can also constrain $T_{eff} \geq 38000\text{K}$. Discrepancies still exist between some of the observed and model line ratios, but the most obvious tend to be the mid-IR observations.

1 INTRODUCTION

Ultracompact (UC) HII regions are generally held to be unevolved nebula marking the site of a young OB star, or group of such stars. The definition of the UC phase is usually taken to be $n_e > 10^4\text{cm}^{-3}$ and $r < 0.1\text{pc}$. (Habing & Israel 1979). Although masked in the visual by the extinction due to the molecular cloud in which they form, they are extremely luminous objects in both the infrared and radio wavebands. Interest in this area has been renewed with the completion of a sparsely sampled VLA survey of the galactic plane by Wood & Churchwell (1989). They found that the numbers of UC HII regions they detected were inconsistent with the simple picture in which the Strömgren radius expands at the sound speed of the region, and hence expands to be larger than 0.1pc after $\sim 10^4$ years (see, eg., Osterbrock 1989).

There are several more complex models that would explain the observed numbers. Van Buren et al. (1990) have suggested that an O star may be formed with a peculiar velocity relative to its natal molecular cloud. The stellar wind known to exist in main sequence OB stars supports a bow-shock ahead of it as it passes through the molecular cloud. The ionisation front is trapped and the region is constrained from expanding by this motion. In another scenario (e.g. Keto, Ho & Haschick 1987), material in the molecular cloud is still infalling into the HII region, again constraining the growth of the Strömgren radius. Hollenbach, Johnstone

& Shu (1993) have proposed that a remnant circumstellar accretion disk may replenish the nebula with new material, hence intercepting much of the far UV light from the exciting star. Dyson, Williams & Redman (1996) advanced a somewhat similar model, in which the interaction of the stellar wind with a clumpy molecular cloud can lead to mass loading in the wind, creating the same effect as in the Hollenbach et al. model. All of these models can satisfy the lifetime arguments, but all differ in the other physical properties of these regions (eg. the dynamical structure).

The advent of near-infrared array spectrometers has made it possible to obtain spectra of bright nebular sources with a signal-to-noise that would have been impossible before. Although compact HII regions have been observed widely in the near infrared in the past (see below), only very bright features with high equivalent width have been detected. There are also many intrinsically fainter features that could be present. By studying these we can accurately determine the extinction to the HII region, the conditions present in the regions of different ionisation, examine the impact of the large opacity in the HeI triplet 1.083 μm 2³P–2³S transition on the weaker HeI lines present in the near-IR, and perhaps find transitions that may indicate the presence of bow-shocks (coronal lines are expected to be detectable in these models) or remnant accretion disks (strong neutral transitions or perhaps CO emission).

We have therefore carried out a series of observations of one of the most luminous sources in the VLA survey of Wood & Churchwell, G45.12+0.13. This ultracompact HII region has been well studied at many wavelengths, both prior to and since the Wood & Churchwell survey. There have been observations of the hot excited molecular gas around the region (eg. Churchwell, Walmsley & Wood 1990, Cesaroni et al. 1991), of the continuum emission both at mm and sub-mm wavelengths (Hoare, Roche & Glencross 1991, Wood, Churchwell & Salter 1988, Wood et al. 1988), and of the radio recombination lines (Garay, Reid & Moran 1985, Churchwell et al. 1990). Wood & Churchwell classify this source as ‘cometary’ (with a bright bow-shaped ionisation front in the radio map), but, as Colgan et al. (1991) note, it can also be modelled as a core-halo source, since there is considerable extended emission beyond the bright core observed by Wood & Churchwell (Matthews et al. 1977, Wink, Altenhoff & Mezger 1982). Herter et al. (1981) collected the results of all the near-infrared spectroscopy carried out on this source with the first generation of low resolution instruments. Since then it has largely been overlooked in this waveband, though it has been observed in the mid and far-infrared using both IRAS and the KAO (Simpson & Rubin 1990, Colgan et al. 1991).

The best models of G45.12+0.13 show a core with a density $n_e > 10^4 \text{ cm}^{-3}$, and a lower density halo that may reflect the fact that the ultracompact HII region is embedded in a larger ionised zone (eg. Colgan et al. 1991). Wink et al. (1982) determine the electron temperature to be $T_e = 8000 \pm 2000 \text{ K}$, in agreement with the data from Wood & Churchwell.

This paper presents our results for the 0.85–2.5 μm region. In section 2, we detail the observations made, and the data reduction techniques involved. In section 3, we present the spectra of G45.12+0.13, and identify spectral features. In section 4, we discuss the properties of the identified lines, and from these discuss the possible conditions within the nebula. Finally, in section 5, we present the conclusions of this work.

2 OBSERVATIONS

The data for this paper were accumulated over a period of time, under varying conditions. The initial observations were made at UKIRT with the common user infrared array spectrometer CGS4 (Mountain et al. 1990). CGS4 used a SBRC InSb 62×58 array sensitive from 1–5.5 μm . In all cases the spatial resolution was $3''$ per pixel, and the slit-width was also $3''$. The slit was oriented north-south, across the peak of the infrared emission. We summed over five rows to obtain total fluxes for the object, so that, for the data presented here, each spectral point corresponds to a $3'' \times 15''$ pixel spatially. Since the slit in CGS4 is only one pixel wide, the array is stepped to provide properly sampled spectra. Our data are sampled 4 times over 2 pixels. Details of the dates of observation, the wavelength range covered, the resolution, the actual on-source integration times and the airmass at the time of observation are given in Table 1.

We also obtained a slightly lower signal-to-noise *IJHK* spectrum with the common user infrared imaging spectrometer IRIS on the AAT. IRIS uses a Rockwell HgCdTe

128×128 array sensitive out to 2.5 μm . A detailed description of IRIS can be found in Allen et al. (1993). In this case the slit width was $1.5''$ and we summed over four pixels ($3.2''$) spatially. Details of these observations are given in Table 2.

In addition, we will also refer to data on this object taken for other projects. These include a Br γ image of G45.12+0.13 taken with IRIS, with a spatial resolution of $0.25''$ /pixel, and a high resolution spectrum taken with CGS4 and the echelle grating (resolution ~ 16000) centred on Br γ (see also Lumsden & Hoare 1995).

For data obtained in 1991, conditions were non-photometric and the seeing was poor. The atmospheric standard used was BS7332, an A2V star: it was observed both before and after the observations. To compensate for the air-mass corrections, we averaged the two observations and used that as the standard for the object. Further observations of two K0III stars showed that this resulted in a reliable atmospheric standard. For the 1992 observation, the atmospheric standard used was SAO104728, an A2 star. The UKIRT flux standard, GL748 was also observed, and provides a reliable check of the atmospheric cancellation short of 2.25 μm (there are several absorption features in the flux standard beyond this). For the 1993 data, BS7332 was used as the atmospheric standard, and GL748 was again observed to provide accurate photometry and to enable spurious features in the final spectra caused by intrinsic absorption features in the standards to be allowed for. Conditions were photometric for both the 1992 and 1993 observations, though the seeing was slightly poorer for the latter. The last segment of data taken on 1993 April 4 (from 2.3–2.5 μm) is considerably poorer as it was taken during sunrise when the night sky lines were increasing rapidly in flux. Wavelength calibration was achieved using either krypton or argon arcs for the 1–1.2 μm , 1.6–2.1 μm and 2.3–2.5 μm data, and bright sky lines for the 1.2–1.6 μm and 1.9–2.3 μm data (line wavelengths were taken from the list of Oliva & Origlia, 1992). For the IRIS data the G dwarf BS7644 was used as both a flux and atmospheric standard, and wavelength calibration was by means of an argon arc lamp.

All UKIRT data were taken by nodding along the slit to provide a sky frame taken at the same position on the chip as the object. The object was moved between 27 and $30''$ on the chip in the process. This procedure aids considerably in removing residual sky features, which cancel when the positive and negative beams are added at the end of the data reduction. For the IRIS data, the same procedure was used but the nod distance was considerably less since the slit is only $12''$ long. Given the highly peaked spatial profile of G45.12+0.13, this method gives reliable core fluxes.

The reduction procedure for the CGS4 data followed a standard procedure. First, the sky frames were subtracted from the corresponding object frame. A polynomial fit in the spectral direction was then made to remove the residual sky lines. The rows containing the positive and negative beams were then removed. Since CGS4 fully samples the resolution element by stepping the array, variations in seeing or poor photometric conditions can result in the four sub-spectra having different recorded count levels. This is corrected for by folding the combined spectrum over a period of 2 pixels to provide a ‘ripple-spectrum’, which the object spectra are then divided by. The resultant data were then coadded, leaving for any object two summed spectra corresponding to the

original positive and negative beams. We interpolated over hydrogen absorption lines in the A-type standards (the only feature present in their spectra) by fitting Lorentzian line profiles. The separate halves of the data were then divided by the same beam from the standard (which corrects for differences observed in the overall raw count level in the two beams), and then coadded. Finally spectra were then corrected for the black-body shape of the standard, and flux calibrated where appropriate. Data from non-photometric nights were calibrated by forcing the continuum in the overlap between spectra to match. In doing this, we have assumed that our best photometry occurs in the 1.6–1.8 μ m segment of the final spectra. Small differences (< 5%) found in the continuum level from flux calibrated regions were also removed in the same way. Unfortunately, this procedure is inapplicable in the overlap between *J* and *H*, where the atmospheric transmission is very poor. For this reason we obtained the IRIS spectra as well, and the overall shape agrees well in both data sets. We are confident that each segment is calibrated accurately to within 10% of its neighbour.

IRIS echelle data is considerably different from CGS4 data in that the echelles are cross-dispersed to obtain complete coverage of *IJ* or *HK* in a single exposure. Therefore corrections for curvature of the echelle orders have to be applied before raw spectra can be extracted. Furthermore, since the slit in IRIS is fully sampled by the chip there is no need to correct for variable transmission between sub-spectra as was the case with CGS4. Lastly, given the short length of the slit it was impractical to model residual sky emission, and we were forced to rely on nodding along the slit to remove the sky features. In other respects the data were treated in the same fashion as the CGS4 data.

Allowance must also be made for the deep atmospheric absorption features between 1.85 and 2.08 μ m and between 1.35 and 1.45 μ m, which are primarily caused by atmospheric water vapour and CO₂. The difference between a good high altitude site such as Mauna Kea and a lower altitude site such as Siding Spring is clearly evident in the much poorer spectra obtained through these regions with IRIS. In particular, the CGS4 data acquired on the night of 1993 April 4 are almost photometric through the gap between H and K windows, showing that the column density of water vapour was especially low. However, despite this, we assume that the lines that fall in these wavelength ranges are of essentially lower photometric accuracy. The quoted errors from the line fits described below are therefore likely to be very much a lower bound to the true error.

For one line we have attempted to model the atmospheric response to remove this uncertainty. The HeI 2¹S–2¹P transition at 2.058 μ m falls in the midst of CO₂ absorption. The intrinsic width of the absorption features are very narrow, as are the intrinsic line widths of the HII region. Therefore, at different times according to the object's velocity with respect to the earth, more or less of this flux can be absorbed by the CO₂ features. We therefore applied the corrections described in Doherty et al. (1993) to derive a better estimate of this line. We observed the HeI line on two separate occasions with CGS4. The respective corrections we derive are 1.152 and 1.252 for the 1992 November 15 and 1993 April 4 CGS4 data respectively. After correction, the difference in the observed line flux between the two nights is less than their respective errors. We therefore find this

procedure to be reliable and quote the mean of these fluxes in Table 3.

3 THE STRUCTURE OF G45.12+0.13

In Figure 1, we display a grey scale plot of the Br γ image obtained with IRIS. The pixel scale is 0.25arcsec/pixel, and the seeing was \sim 1arcsec at K. The image is not flux calibrated. The underlying continuum has not been subtracted but, as will be shown later by the spectra, this continuum is largely free-free dominated in any case. We can compare this image with the 15GHz radio map presented by Wood & Churchwell (1989). The general outline shown by the radio data maps well onto the higher contours of the IR data. However, the Br γ map shows considerably more extended structures around these.

The similarity of the two maps indicates that the extinction across the HII region is largely uniform. This is confirmed by the lack of evidence for variations in the extinction from our long slit spectroscopy (see section 5.1). However, for a proper comparison we must also ensure that the radio continuum emission is not optically thick. As shown by Wood & Churchwell, many UC HII regions are still marginally optically thick even at 15GHz, and although there is no evidence for this in G45.12+0.13 when averaged across the whole nebula, it may still be true near the core. To assess the likelihood of this we compared the cross-sections through the peak of the emission in both the radio and the near-IR. This reveals very similar profiles in both: the radio core can be fit reasonably by a Gaussian of full width at half maximum of 1.1'' and the IR core by a Gaussian with 1.75''. Taking account of the seeing at K and possible positioning errors in taking these sections, these profiles are consistent. This implies that any residual opacity in the radio must be small, as expected. We can also show this by comparing the the peak flux per beam quoted by Wood & Churchwell (1989) at 5 and 15GHz. From this it seems very likely that $\tau_{15\text{GHz}} \ll 0.1$. The slight differences in beam sizes and the slight misalignment of the peak locations at the two frequencies do not allow us to say more than this however. It is clear however that the opacity at 15GHz is sufficiently small that we can ignore it in what follows, and we can treat the 15GHz radio map and the near-IR spectra and image as tracing the same structures.

Lastly, we note that the total structure of G45.12+0.13 is not remarkably cometary, as Wood & Churchwell have claimed, but is rather more amorphous. This is consistent with the model fit of Colgan et al. (1991), and it seems unlikely that the bow-shock hypothesis of Van Buren et al. applies to this source on this basis alone.

4 THE SPECTRUM OF G45.12+0.13

The CGS4 spectra are shown in Figure 2, and lines identified are given in Table 3. The region from 0.9–1.0 μ m is taken from our IRIS spectra, scaled by the relative strength of Pa β in the CGS4 and IRIS data to give an indication of the strength of the [SIII] lines. The weaker lines are more readily seen in Figure 4 where the strong lines have been suppressed to show the continuum in more detail. We do

not otherwise show the IRIS spectra separately, but the line strengths measured are also given in Table 3.

The lines were fitted with either a single triangle, or in the case of blends, two triangles. This is the correct function to fit for an unresolved line with CGS4 (or IRIS) and was found to be satisfactory for virtually every feature. Where complex blends of more than 2 lines occurred, trying to fit more than two triangles to the observed profile was largely unsuccessful (though we did adopt this approach for one blend – see section 5.4). We give wavelengths as measured from these fits, but, with the exception of highly blended lines, the errors on these fits are not a realistic measure of the true observational error: for the signal-to-noise achieved in these observations, the typical ‘true’ error on the observed wavelength is approximately a tenth of a resolution element. Therefore, we quote this error, $\delta\lambda$, unless the actual error on the fit is worse than this (which only occurs with highly blended lines). Note that the wavelength calibration beyond $2.3\mu\text{m}$ has an offset present. We have checked the line identifications against the known wavelengths of the HI Pfund series to correct for this. Marginally detected lines are included in the list: caution should be used in interpreting such features. Lines which are sufficiently blended that they cannot be resolved are marked by *bl* after the wavelength as well. Where we cannot deblend these features with any confidence, the flux is also marked with a *bl* and indicates that this is the total flux in the blend.

The identification of each feature is also given in Table 3. Lines for which we are unsure of the identification are marked by a ? in this column. As one might expect, most of the bright features arise from hydrogen recombination lines. The only lines of comparable strength are the HeI 2^3P-2^3S $1.083\mu\text{m}$ metastable triplet ‘ground-state’ and the singlet 2^1P-2^1S $2.058\mu\text{m}$ transition and the [SIII] lines at 9535\AA and 9072\AA . Amongst the weaker features, the most common are the other low- n HeI recombination lines not coincident with hydrogen lines, and many transitions from the low lying [FeII] multiplets.

Line fluxes are taken from the fitting procedure, as are the quoted errors. It should be noted that our data spans regions of very low atmospheric transmission (primarily the gap between the *J* and *H* windows, between *H* and *K* and the region from $1.1-1.2\mu\text{m}$). Our IRIS data are unreliable in these regions and no line strengths are quoted. The fluxes quoted for lines in our CGS4 data should also be treated with caution in these regions, and true errors on the line fluxes are unlikely to be well represented by the fitting process. The fluxes listed are all scaled relative to $\text{Pa}\beta$, and all have been corrected for extinction using the extinction curves derived in section 5.1. The original observed line fluxes can be regained by using the appropriate parameters in the extinction curve, the value of the $\text{Pa}\beta$ flux after correction for extinction given in Table 3 and the strengths of the other lines given there also. For highly blended lines the quoted fluxes may also be in error. The total flux in the blend however should be reliable. The ‘true’ error in any given line can be estimated by comparing the differences in the ratios of the HI series between the IRIS and CGS4 data, though it should be noted that this may reflect real changes across the face of the nebula since the slit aperture and position angle is different for the CGS4 and IRIS data.

5 PHYSICAL CONDITIONS WITHIN G45.12+0.13

5.1 Extinction

Typically the near infrared extinction law is derived by assuming that the dust opacity follows a power law: ie. if $\kappa_{\text{dust}} \propto \lambda^\alpha$, then the differential optical depth between two lines,

$$\Delta\tau_{12} = -\ln \frac{[I(\lambda_2)/I(\lambda_1)]_{\text{obs}}}{[I(\lambda_2)/I(\lambda_1)]_{\text{theory}}},$$

is equivalent to

$$\Delta\tau_{12} = \tau_{\lambda_1} [(\lambda_2/\lambda_1)^\alpha - 1].$$

Obviously, in the case where we know α and have a measurement of a line (or free-free processes) where $\tau = 0$, we can derive τ at the wavelength of the line absolutely.

The extinction can be derived in several different ways. First, we can compare the observed line fluxes with the radio continuum, which arises from free-free emission. The expected radio emission can be calculated as shown by Rubin (1968), and the expected line flux can also be derived using the calculations of Hummer & Storey (1987). Combining these we get in the general case (assuming the nebula is ionisation bounded and there is no He^{++} , which are reasonable in this case)

$$F_{Br\gamma, \text{theory}} = 2.45 \times 10^{13} S_\nu \nu^{0.1} T_4^{0.35} j_{Br\gamma} \text{Wm}^{-2},$$

where S_ν is given in Jy, ν in GHz, T_4 is in units of 10^4K and $j_{Br\gamma}$ is in Wm^{-3} and is taken directly from Hummer & Storey. For $n_e = 10^5\text{cm}^{-3}$ and $T_e = 7500\text{K}$, $j_{Br\gamma} = 4.64 \times 10^{-28}\text{Wm}^{-3}$.

We estimated the total radio flux within the infrared slit from the Wood & Churchwell radio maps. However, since we observe hydrogen emission beyond the lowest contour in their radio maps, it is clear that their data is not sensitive to low level large scale emission (the VLA configuration used is insensitive to structures on scales larger than $10''$). Therefore, to minimise the errors in carrying out this procedure, we have only used data corresponding to the emission peak: in practice this is defined by the $0.8'' \times 1.5''$ aperture of IRIS (1×2 pixels) for which we observe a $\text{Br}\gamma$ flux of $(1.6 \pm 0.02) \times 10^{-15}\text{Wm}^{-2}$. We estimate the total radio flux within this aperture as 525mJy at 2cm (assuming a Gaussian profile for the core of the radio emission with $\sigma \sim 0.5\text{arcsec}$ and the peak flux given by Wood & Churchwell 1989). Hence combining this with the 15GHz data of Wood & Churchwell gives:

$$F_{Br\gamma, \text{theory}} = 7.1 \times 10^{-15}\text{Wm}^{-2}.$$

Allowing for errors in the radio flux (resulting both from our assumptions and from possible mismatch between the centreing of the apertures) and the electron temperature, the total error in this flux is $\sim 30\%$. Hence $\tau_{Br\gamma} = 1.49$, with a likely error of ~ 0.3 . We have assumed in this that the 15GHz emission is optically thin: free-free opacity will result in a larger value of $\tau_{Br\gamma}$ than given here. However, for the estimate of the free-free opacity at 15GHz given in section 3, the difference is essentially within the error quoted.

Secondly, we can compare the hydrogen line ratios themselves. This is the method recommended by Landini et al. (1984) for measuring the extinction law in a more general

case. It has the advantage that we can derive both τ and α since we have many recombination line measurements. The model data has been taken from the case B recombination line predictions of Hummer & Storey (1987), where again we have used $T_e = 7500\text{K}$ and $n_e = 10^5\text{cm}^{-3}$ (the values are only slightly sensitive to density within the range in question but are sensitive to electron temperature). The observed fluxes for the Pfund, Brackett and Paschen series lines observed with CGS4 are plotted in Figure 3a, together with the model values derived from Hummer & Storey. Figure 3b shows similar data derived from our IRIS observations.

With these assumptions we find $\tau_{\text{Br}\gamma} = 1.45 \pm 0.06$ and $\alpha = -2.01 \pm 0.06$ from our IRIS data, and $\tau_{\text{Br}\gamma} = 1.35 \pm 0.04$ and $\alpha = -2.01 \pm 0.05$ from our CGS4 data. In carrying out the fits we have excluded those points lying in regions of poor atmospheric transmission, and those which are blended with other features. The fits have reduced χ -squared values of 0.9 and 2.2 respectively. The better fits obtained with IRIS highlight the problems in accurately matching segments of CGS4 data taken at different epochs. In particular, the data between $1.5\mu\text{m}$ and $1.6\mu\text{m}$ can be seen to be slightly offset from the longer wavelength CGS4 data. These fits give a predicted visual extinction of $A_V = 23\text{--}25$. The exact agreement between $\tau_{\text{Br}\gamma}$ from our IRIS measurements and from the radio data must be seen as being somewhat fortuitous given the assumptions we have made. All values of α and τ that we derive are also compatible with our non-detection of the higher members of the Paschen series. Since the values of $\tau_{\text{Br}\gamma}$ agree within the errors for the two data-sets we conclude that there is no evidence for strong deviations in the extinction across the face of the nebula. Similarly, we see no evidence that the value of $\tau_{\text{Br}\gamma}$ changes along the slit for our CGS4 data.

Since the interpretation of the HeI line spectrum is complicated (see section 5.2), it is inadvisable to use HeI line ratios in deriving estimates of the extinction. The one exception to this is the $4^3\text{P}\text{--}3^3\text{D}/4^3\text{P}\text{--}3^3\text{S}$ pair which have a common upper level. However, since the former line falls in a region of poor atmospheric transmission, the result again has a large error. Using the IRIS data, we derive $\tau_{\text{Br}\gamma} = 1.55 \pm 0.2$, assuming $\alpha = -2.01$. This error is likely to be somewhat conservative, given the comments above on the photometric accuracy of any line that falls between 1.8 and $2.06\mu\text{m}$. However, the result is consistent with the assumed slope. Using the CGS4 data, the derived $\tau_{\text{Br}\gamma} = 1.38$, again consistent with our earlier result.

Lastly, we can compare line ratios of other ions. The ratio of [FeII] $1.257\mu\text{m}$ to [FeII] $1.644\mu\text{m}$ is a potentially powerful indicator of extinction since the two lines have a common upper level. In practice, since the $1.644\mu\text{m}$ line is heavily blended with Br12, the uncertainty introduced is large. We discuss the ratios of these two lines further in section 5.3. One other potential indicator is the ratio of the [SIII] $^1\text{D}_2\text{--}^3\text{P}_1$ and $^1\text{D}_2\text{--}^3\text{P}_2$ lines at 9072\AA and 9535\AA , since these also share a common upper level. As shown in section 5.4, the derived extinction from these lines agrees well with that derived from the HI lines.

Although the values of $\tau_{\text{Br}\gamma}$ measured by the two instruments are statistically equivalent, it is possible that there are variations in the measured τ due to variations in the optical depth through the dust along the line of sight. Natta & Panagia (1984) outline the expected observed versus in-

trinsic extinctions in the general case of an inhomogeneous screen. For the small values of τ observed, a change of $\sim 10\%$ in these values as measured between a small aperture (essentially closer to the ‘intrinsic’ value) and a large aperture (covering most of the source as is the case for our CGS4 data) is entirely possible if we imagine the dust screen as existing in a thick shell around a mostly spherical HII region (equivalent to the $n = 1$ case of Natta & Panagia). However, plotting $\log \tau$ (derived by comparing the IR fluxes with those expected from the radio for all λ) as a function of $\log \lambda$ as they do (cf their figure 10), shows no evidence for a turnover towards a flatter slope at shorter wavelengths, which would be the characteristic for such behaviour. Since we do not see any of the optical HI lines however, it would be difficult to fully test the ‘clumping’ model from the data available to us at present. It is clear though that the slope we measure should only relate to the intrinsic extinction present.

Previous extinction estimates for this source have ranged from $A_V = 10 \rightarrow 30$, as discussed by Hoare et al. 1991. They express concern that the hydrogen recombination line strengths may be affected by stellar winds based on the broad HI lines detected in the high resolution observations of Tanaka et al. (1985). However, a velocity resolved spectrum of the Br γ line shows that the intrinsic width is $\sim 45\text{kms}^{-1}$, and we therefore reject the Tanaka et al. result as incorrect. We conclude that G45.12+0.13 has an extinction curve that is somewhat steeper than that found in optically visible nebulae such as reported by Landini et al. In what follows, we assume the use of the extinction curve derived from the HI series to deredden our data, with $\alpha = -2.01$ for both the IRIS and CGS4 data, and with $\tau_{\text{Br}\gamma} = 1.45$ for the IRIS data and $\tau_{\text{Br}\gamma} = 1.35$ for the CGS4 data.

5.2 Helium Recombination Lines

Basic recombination line strengths for the infrared HeI lines are presented by Smits (1991a,b), for the case of 10% helium abundance. There are several effects that are not included in this model however. These include collisional excitation from the 2^3S metastable level to levels higher than $n = 3$, photoionisation of the 2^3S level (Clegg & Harrington 1989), the inclusion of the role of the optically thick $n^3\text{P}\text{--}2^3\text{S}$ series (Robbins 1968) and the role of dust and hydrogen in absorbing scattered $2^1\text{P}\text{--}1^1\text{S}$ photons resulting in a breakdown of the case B approximation to a small extent (Doyon, Puxley & Joseph 1992, Shields 1993). Of these, we can discount photoionisation as an important factor from the work of Clegg & Harrington. Their model of the low excitation compact planetary nebulae IC418 is a reasonably close approximation to the situation in G45.12+0.13 and, as they show, collisional excitation of the lower singlet levels dominates over photoionisation as a means of depopulating 2^3S . For the other possible contributing effects, since we have accurate fluxes for a number of the low lying HeI transitions, we can directly test for their presence.

Table 4 gives the ratios of the observed HeI lines with the $4^3\text{D}\text{--}3^3\text{P}$ line. This latter line arises from the same state as the more commonly used 4471\AA $4^3\text{D}\text{--}2^3\text{P}$ transition that is well known to be largely unaffected by either collisions or significant line opacity (eg. Clegg 1987). Table 4 also gives

the theoretical ratios as taken directly from Smits (1991b): with the exception of the $2^{1,3}\text{P}-2^{1,3}\text{S}$ transitions, these represent the values derived from direct recombination and cascade processes only. The values are for $T_e = 10^4\text{K}$ and 5000K , and $n_e = 10^4\text{cm}^{-3}$. Changes in the electron density have a negligibly small effect on the values tabulated by Smits for all line ratios except those involving the $2\text{P}-2\text{S}$ transitions. Smits includes collisional excitation processes for these lines in his predictions. The electron temperature for G45.12+0.13 will lie somewhere between these limits as noted previously.

The measured flux for the $4^1\text{P}-3^1\text{S}$ line assumes that the contribution from HI Br22 can be derived from the measured Br21 flux and the ratio of Br22/Br21 as derived from Hummer & Storey for $T_e = 7500\text{K}$. The $5^{1,3}\text{F}-3^{1,3}\text{D}$ lines are also heavily blended with both Pa β and the $a^4\text{D}_{3/2}-a^6\text{D}_{3/2}$ transition of [FeII]: there is a considerable difference seen between the ratio observed with CGS4 and that with IRIS, so we conclude that the quoted flux of this line is unreliable. The $7^3\text{P}-4^3\text{S}$ line at $1.745\mu\text{m}$ is coincident with the $a^4\text{D}_{1/2}-a^4\text{F}_{3/2}$ [FeII] transition: again the ratio is likely to have a larger error than that quoted. Lastly, the $5^3\text{P}-3^3\text{D}$ line is blended with both the [FeII] $a^4\text{D}_{3/2}-a^6\text{D}_{1/2}$ and $a^4\text{D}_{5/2}-a^6\text{D}_{5/2}$ transitions and may also have a larger error than quoted. The $2^{1,3}\text{P}-2^{1,3}\text{S}$ lines are discussed in greater detail below. The $4^1\text{P}-3^1\text{S}$ agrees well with the theory, after making the correction for the HI contribution to the blend, but the $4^1\text{D}-3^1\text{P}$ line at $1.909\mu\text{m}$ does not. It falls on the edge of the deep atmospheric OH absorption band however. The $5^3\text{D}-3^3\text{P}$ transition also agrees well with the theory. However, the $4^{1,3}\text{S}-3^{1,3}\text{P}$ blend shows some enhancement compared to expectation, and the $4^3\text{P}-3^3\text{S}$, $5^3\text{P}-3^3\text{D}$, $7^3\text{P}-4^3\text{S}$ and $4^3\text{P}-3^3\text{D}$ are all significantly enhanced over the expected recombination values.

The only mechanisms other than recombination for populating the higher n levels are opacity in the $n^3\text{P}-2^3\text{S}$ series and collisions from 2^3S . Since the observed ratios and theoretical ratios are most discrepant for those lines which originate from $n^3\text{P}$ levels this is strongly suggestive of high opacity. Collisions would preferentially enhance $\Delta L = 0$ transitions more than any others. We can quantify the relative importance of collisions to these higher n levels in the same manner as Clegg (1987). For the case of collisional excitation of 4^3S from 2^3S , we find the collisional excitation rate to be $\sim 10^{-12}\text{cm}^3\text{s}^{-1}$. The effect this has on the $4^3\text{S}-3^3\text{P}$ transition can then be calculated by considering the comparative importance of recombinations and collisions to populating 4^3S . The ratio of excitations by collisions to those by recombinations is simply just $N(2^3\text{S})k_{eff}/N(\text{He}^+)\alpha_{eff}$. The relative population of the 2^3S level is taken from Clegg (1987), α_{eff} is derived from the values in Smits and k_{eff} is derived from the collision strengths of Sawey & Berrington (1993), scaled by the branching ratio of the $4^3\text{S}-3^3\text{P}$ and $4^3\text{S}-3^2\text{P}$ transitions. This implies that only ~ 3 in every thousand $2.1128\mu\text{m}$ $4^3\text{S}-3^3\text{P}$ photons arise from collisions.

The optical depth in the core of the $2^3\text{P}-2^3\text{S}$ $1.083\mu\text{m}$ line can be estimated crudely by assuming a typical density of 10^4cm^{-3} , a core radius of 0.02pc (determined from our fit to the radio data in section 3 above), and purely thermal line broadening: from this we derive $\tau(1.083) \sim 400$, or $\tau(3889) \sim 20$. Such values would imply that even the $7^3\text{P}-2^3\text{S}$ line has an opacity ~ 1 . Robbins (1968) gives the ex-

pected line enhancements for a few of the stronger infrared lines as well as the dominant optical transitions. We have assumed the case of purely thermal line broadening, even though we know this to be incorrect from the observed line widths in G45.12+0.13, since we do not know what component of the observed line broadening is due to real velocity shifts (which would have a major impact as noted by Robbins) and what is due to turbulence (which would have less of an effect).

From these data we can derive expected line enhancements for all the lines that do not originate from $n^3\text{P}$. The ratio of the enhancement over the original recombination line flux is the same for all transitions from any given state. Therefore, to calculate the enhancement in the $4^3\text{S}-3^3\text{P}$ transition, we only require to know the enhancement in the $4^3\text{S}-2^3\text{P}$ transition which is given by Robbins. In this way we also correctly account for cascades from higher levels into 4^3S . This gives the enhancement as $\sim 33\%$, in agreement with what is observed. Similarly, those lines arising from $n^3\text{D}$ should show negligible enhancement ($<5\%$ for both $4^3\text{D}-3^3\text{P}$ and $5^3\text{D}-3^3\text{P}$), again in agreement with what is observed.

For the lines that do arise from $n^3\text{P}$, we adopted an alternative approach, since the quoted line fluxes in Robbins relate to the optically thick lines. If we assume that all the light in the $n^3\text{P}-2^3\text{S}$ lines is redistributed into other lines arising from the same $n^3\text{P}$ state (as a first approximation), then the ratio of the extra flux to the original recombination line flux is simply given by the ratio of all the branching ratios from that state to the branching ratios of all those transitions except the $n^3\text{P}-2^3\text{S}$ one. We can compare the numbers we derive with the two cases given by Robbins for near-IR lines. This is a reasonable approximation in this case since cascades from higher optically thick transitions are less important in feeding these transitions than for those lines arising from outside $n^3\text{P}$. For 4^3P this leads to a predicted enhancement of a factor of 4.6, for 5^3P a factor of 3.4 and for 7^3P a factor of 2.6. By comparison, Robbins quotes an enhancement for $4^3\text{P}-3^3\text{S}$ of 4 and for $4^3\text{P}-3^3\text{D}$ of 3.5 for the case where $\tau(3889) = 75$. Although our crude estimates are somewhat too high, they are clearly close to the ‘true’ estimates when the line is truly optically thick. The actual observed enhancements for the transitions originating from 4^3P and 5^3P are ~ 4 in reasonable agreement with what is observed. The observed enhancement for the $7^3\text{P}-4^3\text{S}$ line is ~ 7 , much larger than expected. This is the only truly discrepant line however, and as noted above, is completely blended with an [FeII] transition.

As shown by Clegg (1987), at high electron density, the $2^3\text{P}-2^3\text{S}$ line is dominated by collisional excitation (by a factor of ~ 5 from his data). Collisions between the $n = 2$ levels are explicitly allowed for by Smits, and we also find substantial agreement with his data for the adopted value of T_e and n_e . The $2^1\text{P}-2^1\text{S}$ line is also considerably modified from its pure recombination value. In this instance resonance scattering of the 584\AA $2^1\text{P}-1^1\text{S}$ line can lead to additional $2^1\text{P}-2^1\text{S}$ photons. However, $2^1\text{P}-1^1\text{S}$ photons can ionise hydrogen and be destroyed by dust as well. In addition, the population of the 2^1S level can also be raised by collisional excitation from 2^3S . As shown by Shields (1993), this problem must be treated using a full radiative transfer model to correctly model the expected $2^1\text{P}-2^1\text{S}$ line flux as a function of the stellar effective temperature. The major dif-

ference between that work and more simplistic calculations (eg. Doyon et al. 1992) is that Shields predicts the ratio of the $2^1\text{P}-2^1\text{S}$ with $\text{Br}\gamma$ decreases above 40000K rather than saturating when the H^+ and He^+ zones fully overlap. We have already demonstrated an example of such behaviour in a previous paper (Lumsden, Puxley & Doherty 1994). Our observations here are in good agreement with the expected maximum value for the $2^1\text{P}-2^1\text{S}/\text{Br}\gamma$ ratio (we assume the actual maximum value is somewhat better defined by Doherty et al. 1994 than by Shields, since the only case he considers with high density appears to be off the scale on his Figure 1(d)). This leads us to conclude that the exciting stars in G45.12+0.13 must be cooler than $\sim 42000\text{K}$. Lastly, the strength of the $2^1\text{P}-2^1\text{S}$ line indicates that the 2^3S level is predominantly depopulated by collisions, and not photoionisation, in agreement with the model results of Clegg & Harrington (1989).

As a further test of the ratio of He^+/H^+ , we can use the $4^3\text{D}-3^3\text{P}$ transition, since it arises solely from recombination and is straightforward to interpret since the $4^3\text{D}-3^3\text{P}/\text{Br}\gamma$ ratio does saturate once the H^+ and He^+ zones overlap (cf. the discussion of the optical HeI lines in this context in Doherty et al. 1995). The ratio of this line with $\text{Br}\gamma$ gives 0.12 ± 0.01 from the average of our CGS4 and IRIS data. The theoretical value for $T_e = 7500\text{K}$ and $n_e = 10^4\text{cm}^{-3}$ is $1.32n_{\text{He}^+}/n_p V_{\text{He}^+}/V_{\text{H}^+}$. Increasing the density by an order of magnitude causes a drop of $\sim 10\%$ in the theoretical ratio, as does raising T_e to 10000K . Assuming a nominal helium abundance by number of 10% of hydrogen implies that our observed ratio can only be satisfied if the hydrogen and helium ionised regions essentially overlap. An increase in the abundance to 0.12 would cause an increase in the theoretical ratio of 20% , which is 4σ above the observed ratio, but it seems unlikely that G45.12+0.13 has this abundance (Herter et al. 1981). We therefore set a lower bound to the stellar effective temperature for the exciting star(s) in G45.12+0.13 of $\sim 38000\text{K}$. This is consistent with the upper limit derived above from the $2^1\text{P}-2^1\text{S}/\text{Br}\gamma$ ratio. Our result is in disagreement with the inferred HeI/HI ratio derived from radio recombination lines by Wink et al. (1982), which has been used previously in modelling this source. It seems likely that at the densities known to exist in this region both line broadening and maser effects have a significant impact on the measured RRL line strength.

5.3 Forbidden Iron Lines

Since Fe^+ has an ionisation potential of only 16.18eV , it is likely to exist only near the edges of the nebula. The [FeII] emitting zone will coincide both with the H and H^+ (and S and S^+) regions, but sits outside the He^+ , O^{++} and S^{++} zones (all species that have been previously observed either in this work or by Colgan et al. 1991). Since most of the lines that can be seen have critical densities larger than the peak core density observed, we adopted a simple model in trying to interpret the [FeII] lines and assumed that they all arose in the same isothermal, isodensity region. For the temperature we have taken the nominal value of $T_e = 7500\text{K}$ (since electron temperature does not change radically with position in most nebular models). In practice, the variation of most [FeII] line ratios discussed here with T_e is small in any event, since the separation of the first 13 energy levels is

small. The near infrared [FeII] ratios are primarily indicators of electron density.

Collision strengths for [FeII] were updated recently by Pradhan & Zhang (1993) and we use this source in what follows. Transition probabilities were taken from Nussbaumer & Storey (1988). The wavelengths are calculated from the energy level data of Johansson (1978). Table 5 gives the ratios of the observed transitions from $a^4\text{D}-a^6\text{D}$ and $a^4\text{D}-a^4\text{F}$ against the $1.257\mu\text{m } a^4\text{D}_{7/2}-a^6\text{D}_{9/2}$ line. Also given there are the expected theoretical ratios. Of these, the easiest to consider are those transitions that also arise from $a^4\text{D}_{7/2}$. The observable transitions fall at 1.321 , 1.372 and $1.644\mu\text{m}$. The $1.644\mu\text{m}$ line is completely unresolved from HI Br12, and the flux was derived by fixing Br12 relative to Br11 and Br13 using recombination theory, and attributing the residual to the [FeII] line. With this partition the line strength agrees with the theory. This also shows that the [FeII] lines give the same extinction as derived from the HI lines in Section 5.1 above. The other two line ratios are also consistent with the theory.

Use of the other line ratios allow us to predict electron densities, and these are also given in Table 5. Again blended lines are likely to give the largest errors. This is certainly true for the 1.797 and $1.800\mu\text{m}$ lines which are also weak detections. The $1.533\mu\text{m}$ transition is also clearly visible, blended with Br18, and is of roughly the correct strength (predicted to be $\sim 4 \times 10^{-17}\text{Wm}^{-2}$), if we scale Br18 to Br19 and Br17 as we did above for Br12. Lastly, the $1.745\mu\text{m}$ transition is blended with the $7^3\text{P}-4^3\text{S}$ HeI transition. We therefore discount it in this analysis: it is worth noting however, that the maximum contribution from both HeI and [FeII] lines cannot explain the observed flux alone if the atomic data is correct.

The remaining lines can all be fit by gas of moderately high density, $n_e \sim 10^4\text{cm}^{-3}$. Colgan et al. find a core-halo density distribution fits the radio map under the assumption of spherical symmetry. Their halo density is compatible with our derived [FeII] density, which is in line with the expectation that the Fe^+ emitting region should be well away from the exciting source. Lastly, we have estimated expected fluxes for this density for all those lines not seen in our spectra, and find that they are below our detection threshold as expected.

For the four tabulated [FeIII] transitions we used the collision strengths from Berrington et al. (1991) and the transition probabilities from Garstang (1957). From estimates of the expected fluxes it is clear that any other [FeIII] lines in this wavelength region would be unobservable. The observed flux ratios fit the model well if we assume a high density ($n_e > 10^4\text{cm}^{-3}$), except for the $2.3485\mu\text{m } a^3\text{G}_5-a^3\text{H}_5$ line which is too strong. It is likely that this line has substantial underlying emission from the higher members of the hydrogen Pfund series, especially Pf29. Using similar methods to those described above, we can fix the flux in the Pf29 line, and find that it contributes $\sim 50\%$ of the observed flux. The resultant expected strength of the [FeIII] line is then in agreement with the model. The errors on the data however preclude the use of this ratio as an accurate measure of the density but the lower limit derived is consistent with the expected maximum electron density from the radio data.

Unfortunately it is not possible to use forbidden iron

lines as probes of the ionisation structure of the nebula since the next stage, Fe^{3+} , does not have transitions in the near infrared, and the stage after that has an ionisation potential higher than He^{2+} which is not observed in this nebula. It is likely that the dominant ionisation stage in the nebula is Fe^{3+} as seen in the model HII region of Oliva, Moorwood & Danziger (1989).

5.4 Forbidden Sulphur Lines

The [SII] lines of $1.0289\mu\text{m } ^2P_{3/2} - ^2D_{3/2}$, $1.0323\mu\text{m } ^2P_{3/2} - ^2D_{5/2}$, $1.0339\mu\text{m } ^2P_{1/2} - ^2D_{3/2}$ and $1.0373\mu\text{m } ^2P_{1/2} - ^2D_{5/2}$ are highly blended, and it is therefore difficult to estimate their relative line fluxes accurately. Consideration of the atomic data (taken from Mendoza 1983) however, shows that the ratios between the lines should be nearly constant except when $n_e > 5 \times 10^4 \text{cm}^{-3}$. Unfortunately, the individual components are completely unresolved in our CGS4 data, and are of low signal-to-noise in our slightly higher resolution IRIS data. We therefore opted to fit the CGS4 data alone by considering a simultaneous fit to all four lines, with a single line width, and the separations determined by the values above. The results of this fit are given in Table 3. We should note however that small changes in the fit parameters produced little difference in the ‘goodness’ of the final fit, but moderately large changes in the relative line fluxes in the blend. In particular, the strengths of the two closest lines at 1.0323 and 1.0339 μm are somewhat arbitrary, although the total overall flux in these lines together is correct. The theoretical data shows that the ratios of the lines within this blend are all expected to be approximately constant (except at very high density for those arising from different upper levels). Comparison of this data with the observations shows reasonable agreement, within the large quoted errors, for all ratios except those involving the 1.0323 μm line. As noted, the strength of this line is somewhat arbitrary, so we conclude that the theory and observations are in substantial agreement.

We also detect the far-red [SIII] $9535\text{\AA } ^1D_2 - ^3P_2$ and $9072\text{\AA } ^1D_2 - ^3P_1$ lines in our IRIS data. The observed, dereddened line ratio is 2.5 ± 0.4 . The theoretical value is 2.48 (again using data from Mendoza 1983) in excellent agreement with this. Since we see no other features in our far red IRIS spectrum in the range $0.86\mu\text{m}$ – $1\mu\text{m}$, we conclude that the far-red image of Hefele, Wacker & Weinberger (1977) is entirely due to these two lines. This is also consistent with an optical spectrum we have obtained of the $0.76\mu\text{m}$ – $1\mu\text{m}$ region, which shows that the [SIII] line emission has considerable extent along the slit, in agreement with the extended *I*-band object seen by Hefele et al. Our conclusions in this regard are different to those of Hoare et al. (1991): they estimated the contribution to the *I*-band image as being due to nebular continuum, Paschen series HI lines and the two [SIII] lines. The fact that neither of the first two are in fact seen explains why they measure a lower inferred A_v from this procedure. Lastly, we note that our extinction corrected 9535\AA line intensity is $\sim 1.1 \times 10^{-12} \text{Wm}^{-2}$ in a $1.5 \times 3.2 \text{arcsec}^2$ aperture, compared with that of Lester (1979) as reported by Simpson & Rubin (1984) of $1.2 \times 10^{-12} \text{Wm}^{-2}$ in a 30arcsec circular aperture. Given that we see the [SIII] emission as extended, there is clearly a discrepancy between these two values. For comparison, the ratios of HI lines between

our IRIS and CGS4 data are ~ 1.7 . We therefore expect the total [SIII] emergent flux from this HII region is higher than that measured by Lester. Assuming the same scaling holds for [SIII] as for HI (eg. Rubin et al. 1994), then we might expect the total 9535\AA flux in the CGS4 beam to be $\sim 1.9 \times 10^{-12} \text{Wm}^{-2}$. We use this scaling to allow us to compare the [SIII] fluxes with the CGS4 data in section 6, and also in scaling the [SIII] lines for presentation in Figure 2.

Colgan et al. (1991) and Simpson & Rubin (1984) have previously presented fluxes from the mid-infrared [SIII] lines. It is worth examining their conclusions from what we have determined here. They derive an average electron density of $6200 \pm 2800 \text{cm}^{-3}$ from the $18.7\mu\text{m } ^3P_2 - ^3P_1$ and $33.5\mu\text{m } ^3P_1 - ^3P_0$ lines. This is inconsistent with the densities derived by comparing the 9535\AA line with these transitions (both of those give $n_e > 10^4 \text{cm}^{-3}$). There is an alternative measurement of the $18.7\mu\text{m}$ flux from IRAS LRS data. Simpson & Rubin (1990) find a value which is $\sim 50\%$ larger than quoted by Herter et al., though using very low signal-to-noise data. If we accept that this is a limit to the true flux, then it agrees with the Herter et al. value. However, it is clear that both the mid-IR [SIII] lines cannot be correct if we accept that our data and extinction correction are accurate.

5.5 Other Features

We have tentatively identified the line at $1.189\mu\text{m}$ with [FeII] $a^2G_{7/2} - a^4D_{7/2}$ (which has a vacuum wavelength of $1.18847\mu\text{m}$). To obtain an accurate wavelength for this line we made a simultaneous fit to both this feature and the neighbouring HeI $5^3D - 3^3P$ line, and corrected the first wavelength according to the error we found for the HeI line. This gave the ‘true’ wavelength as $1.1884 \pm 0.0002\mu\text{m}$. This is coincident with the expected wavelength of the [FeII] line. Previous studies in this waveband range have often identified a feature at this location as due to $1.1886\mu\text{m}$ [PII] (eg. Rudy et al. 1992). We cannot formally exclude this line as the correct identification on the basis of the observed wavelength therefore, since it is just consistent with the derived error. The [PII] line has a counterpart at $1.1471\mu\text{m}$, with an intrinsic strength which is 2.6 times less (though Rudy et al. derive an observed ratio of 2.1). After including reddening, the observed line would be $\sim 25\%$ of the strength of the $1.1886\mu\text{m}$ line, which should be marginally detectable: no such line is visible however. We note that in at least one other object, the emission line star η Carinae, the same [FeII] line has been identified (Hamann et al. 1994).

The only other features with positive detections in our spectra are those of OI and H_2 . The OI features seen have been discussed previously by Grandi (1980). The most likely cause of such strong permitted oxygen lines is fluorescence. Given the strength of the $4^3S_0 - 3^3P$ line compared to the $3^3D_0 - 3^3P$ line (~ 2.1 times stronger), it is most likely that these features are predominantly excited by UV continuum radiation. Similar situations have also been noted in many planetary nebulae (eg. Rudy et al. 1992).

All of the lines of molecular hydrogen, H_2 , seen in our spectra are blended with other features, with the possible exception of the line seen at $2.285\mu\text{m}$. The H_2 lines are weak in all cases. The relative strengths of the lines appear to agree well with a model in which the H_2 is excited through

UV fluorescence from the hot central star, and in which the ambient cloud density is high, $n_{\text{H}} > 10^5 \text{ cm}^{-3}$ (Sternberg & Dalgarno, 1989: cf the model displayed in their figure 7d). The inferred molecular cloud density is consistent with the results of the C^{34}S observations of hot molecular gas near the core of the region (Cesaroni et al. 1991). Given the low signal-to-noise in the H_2 lines it is not feasible to use the line ratios to do more than assert general agreement with this model however. The one anomalous feature is the strength of the $2.285\mu\text{m}$ line. It is possible that this line is not due to molecular hydrogen, given that it cannot be explained by the models when the presence of $3\text{-S}(2)$ emission would imply the presence of other features in our spectra which are not detected. Geballe, Burton & Isaacman (1991) reached a similar conclusion from a study of planetary nebulae. We note that the second unidentified line they discuss at $2.199\mu\text{m}$ may also be present in our spectrum, as a weak feature is evident at $2.2\mu\text{m}$. Unfortunately that feature is also coincident with $3\text{-S}(3)$ H_2 emission, and our wavelength calibration in this region is insufficiently accurate to truly determine the nature of these lines. The excitation conditions observed in G45.12+0.13 are however very similar to those described by Geballe et al. for the planetary nebulae in which their unidentified features occur. They attribute these features to unidentified fine structure lines arising from an ion with ionisation potential similar to S^{3+} , which may be weakly detected in G45.12+0.13 (Herter et al. 1981, Simpson & Rubin 1990, Hoare et al. 1991).

5.6 Near Infrared Continuum

The major sources of continuum emission in the near infrared are bound-free and free-free emission from the electrons and ions present (H^+ and He^+), the stellar continuum itself, and emission from both hot dust and possibly very small grains out of thermal equilibrium. Figure 2 has been scaled to show the observed continuum as well as the emission features. The presence of the HI continuum is evident from the obvious Brackett and Pfund discontinuities (at 1.46 and $2.28\mu\text{m}$ respectively). We can quantitatively estimate the contribution that the HI and HeI continua make to this by calculating the expected equivalent width of a suitable HI line compared to the continuum. In practice we used $\text{Pa}\beta$ since there is unlikely to be dust emission at $1.3\mu\text{m}$. We modelled the expected bound-free and free-free components in the fashion outlined by Brown & Mathews (1970). The asymptotic expansions for the Gaunt factors given by Seaton (1960) were used. These values agreed to within 1% with the strictly more correct values tabulated by Ferland (1980) at common wavelengths between 0.8 and $2.5\mu\text{m}$. We assumed the HeI continuum was well approximated by scaling the HI continuum, rather than calculating it separately. This gives the $\text{Pa}\beta$ equivalent width as $0.15\mu\text{m}$ when $T_e = 7500\text{K}$ (as usual there is little sensitivity to density in these calculations). The measured equivalent width is $0.09 \pm 0.01\mu\text{m}$. In order to match this width with the HI and HeI continua alone the electron temperature needs to be unfeasibly large ($T_e \sim 20000\text{K}$). We also plot in Figure 2 the expected HI and HeI continua for $T_e = 8000\text{K}$ for comparison. Figure 4 shows the continuum after this free-free component has been subtracted and the residual corrected for extinction. The excess flux near the two HI discontinuities represents

the higher series lines that are completely blended together: the fact that the continuum on each side of these ‘features’ is essentially flat shows that the electron temperature we used is a good match for the object (the best match in terms of this criterion gives $T_e = 8000 \rightarrow 9000\text{K}$ in good agreement with that derived by Wink et al. 1982).

Finally, we have modelled the residual continuum by the mixture of a crude stellar continuum (assumed to follow a λ^{-4} law in this wavelength region) and emission from hot dust, assuming a grey-body law for the emissivity with a power law exponent of one (solid lines in figure 4). Clearly both of these components are required since the residual continuum rises both to the blue and the red. Rather than attempt to find a best fit model (since we have already made several assumptions), our aim here is to show that this mixture is a good match to the residual continuum. The dashed line in figure 4 shows the combination of a power law normalised to fit the continuum at $1.2\mu\text{m}$, and a grey-body normalised to fit the continuum at $2.4\mu\text{m}$. The dust temperature used was 750K : other temperatures produce deviations from the data at $2\mu\text{m}$ and beyond. However, we note that this temperature itself is sensitive to our assumption of the form of the emissivity for the dust, and in particular the power law exponent used therein. Lastly, we note that despite the fact that we can see significant stellar continuum emission in our spectra, there is no evidence for individual stars in the image. It seems likely that the starlight is reflected, most likely by dust within the nebula: only polarimetry would truly prove this however.

6 MODELLING THE EMISSION FROM G45.12+0.13

Detailed models of G45.12+0.13 have been presented previously by Simpson & Rubin (1984), Colgan et al. (1991) and Hoare et al. (1991). The first of these is largely superseded by Colgan et al., who use the same model, but better observational data. However, our data is also superior to the Colgan et al. and Hoare et al. models in several respects: first, we have more accurate measures of the HeI/HI ratio than previously used; secondly, we have been able to relax some of the constraints on the [SIII] lines; thirdly, we have used both the observed total luminosity and number of ionising photons as a constraint (Colgan et al. do not attempt this explicitly); lastly, since we have an accurate measure of the near-IR extinction we can correct these lines properly for the observed reddening.

We used Cloudy version 84.12 (Ferland 1993) to produce a simple photoionisation model with suitable parameters for G45.12+0.13. We used the derived electron density profile of Colgan et al. since our $\text{Br}\gamma$ image is not calibrated. Colgan et al. used a distance to the source of 8.1kpc in their analysis. Available estimates vary from 6.9kpc (Churchwell, Walmsley & Wood 1990) to 9.5kpc (Wink et al. 1982). We will use the distance adopted by Colgan et al. in what follows. We note that if the source were as close as 6.9kpc , then only two O6 stars or one O5 star are required to provide the necessary observed far-IR luminosity. The latter can be ruled out immediately since a star with $T_{\text{eff}} \sim 45000\text{K}$ will produce a significant S^{3+} volume, and the observed mid-IR $[\text{NeII}]/[\text{SIV}]$ ratio indicates this is not true. We therefore

prefer to model the exciting source as a cluster of OB stars, with a mass function as given by Scalo (1986), in which the number of stars per unit mass present scales as $M^{-2.85}$, and use the relationship between bolometric luminosity and mass as calculated by Puxley (1988) from Kurucz (1979) model atmospheres (Cloudy itself uses somewhat more recent Kurucz models). The use of Kurucz models may be problematical in that these models assume line blanketed LTE is a good approximation for calculating the emergent stellar flux, whereas we know that the non-LTE line blanketed calculations are actually required. However, the latter are extremely difficult to calculate and none are widely available.

The key observational constraints that any model has to match can be summarised as follows: from our data the ratios of the different stages of iron and sulphur ionisation, and the requirement that helium be fully ionised; from previous mid-IR data, the ratio of the $10.5\mu\text{m}$ [SIV] to $12.8\mu\text{m}$ [NeII] lines which is a sensitive measure of the stellar effective temperature in this range (this data being taken from the values quoted by Hoare et al. (1991) from unpublished spectra of Roche & Aitken); from far-IR data the strengths of the $33.5\mu\text{m}$ [SIII], $36.0\mu\text{m}$ [NeIII], $51.8\mu\text{m}$ and $88.4\mu\text{m}$ [OIII] lines (all from Colgan et al). From Herter et al. we convert their 2σ detection of [ArII] at $6.99\mu\text{m}$ into a 3σ limit, and adopt their flux for the $18.7\mu\text{m}$ [SIII] line. We also take as an upper limit the flux of the $15.5\mu\text{m}$ [NeIII] line as derived from IRAS LRS data (we derived this limit from the LRS data ourselves, rather than take it from Simpson & Rubin). We consider a reasonable fit any model line which is within a factor of 2 of the observed data, since there are likely to be deviations from the model in any event introduced by our assumption of spherical symmetry. Lastly, the model must also have the correct total luminosity and the correct number of ionising photons (which is equivalent to requiring the actual model electron distribution be the same as the input data from Colgan et al). These parameters are taken to be the total far infrared luminosity ($166 \times 10^4 L_\odot$) and the number of ionising photons ($10^{49.53} \text{s}^{-1}$) required to produce the observed radio flux as quoted by Wood & Churchwell. By definition, this also ensures that we match the observed radio flux density from optically thin free-free emission.

We assumed standard solar abundances since there is little evidence for deviation from these (e.g. Herter et al). We did not use this as a free parameter as Colgan et al. did. We adopt the same extinction curve as Colgan et al. for the mid and far-IR data (see also Simpson & Rubin 1990). The actual values used are given in Table 6. To compare our CGS4 data with the mid and far-IR data we use the ratio of the Herter et al. $\text{Br}\gamma$ flux with our own (1.1): the ratios with $\text{Pa}\beta$ given in Table 6 take this factor into account. Lastly, we included a typical grain population (see Ferland 1993 for more details), but with a dust to gas ratio one tenth of the interstellar value, as found by Hoare et al. to be the best fit to their mm data.

The requirement that we match both the number of ionising photons and the total luminosity is extremely sensitive to the upper and lower mass cut-off we impose on the initial mass function. The number of ionising photons is relatively insensitive to the lower mass limit assumed as long as this is somewhat less than $20 M_\odot$ ($\sim 30000\text{K}$). It is highly sensitive

to the upper mass limit since the the product of the mass function and the expected number of ionising photons from a star of a given mass is roughly constant above $20 M_\odot$. However, the total luminosity is highly dependent on the lower mass cutoff. In practice, unless we truncate the mass function at $\sim 20 M_\odot$, there are insufficient hard UV photons to provide a spectrum similar to that observed, whilst still remaining within the observed total far-IR luminosity. The possibility that such a cut-off may exist in reality is hard to gauge. Carpenter et al. (1993) showed that there is considerable evidence from infrared imaging that massive stars form in clusters that also contain low mass stars. However, Rayner et al. (1991) find that although this is true in general, low luminosity clusters of stars are less common near very massive stars. The example they cite of W3A has a cluster of OB stars similar to that which we find below to give the best fit for G45.12+0.13. Therefore, we adopt this lower mass cut-off for our modelling, and all the models we describe below have essentially this form.

We tried several different models to find a good fit to the data. We varied the upper mass cut-off between stars with effective temperatures of 38000K and 42000K , we allowed for the ‘clumped’ density model of Colgan et al., and we also included a lower density ‘core’ to the HII region to try and match the derived electron density from the [OIII] lines, which Colgan et al. found to be $\sim 3000\text{cm}^{-3}$. Increasing the upper mass limit beyond this range made all the line ratios discrepant. Decreasing the limit below 38000K also made the ratios discrepant. The closest fit to the data that we could find had a cluster in which the hottest star present had an effective temperature of 42000K (or a star of $\sim 50 M_\odot$), with no clumping and with no low density core. The results from this model are given in Table 6. The major discrepancies we find between this model and the data are as follows: we cannot reproduce the observed neon forbidden lines with any degree of accuracy, with the predicted strengths of both the $12.8\mu\text{m}$ Ne^+ line and the $15.4\mu\text{m}$ Ne^{++} line being too great; we cannot produce the correct ratio for the [OIII] lines (not surprising since this model only has low densities at large radius from the stars), leading to the predicted flux of the $88.4\mu\text{m}$ line being too small; as noted in section 5.4, we cannot match all three of the [SIII] features, with the predicted strength of the $33.5\mu\text{m}$ line being half the observed value; the model also overpredicts the rate at which the 2^3S level is photoionised, consequently making the $2.058\mu\text{m}$ line far too weak; lastly, the low ionisation species ([FeII], [SII]) are predicted to be weaker than seen. Correctly accounted for are the strengths of the other sulphur and argon lines, the opacity in the helium triplets, and the helium line strengths other than the $2.058\mu\text{m}$ line and the strength of the stronger [OIII] line and the [NIII] line.

Most of the discrepancies in the model can be set aside. Some are a consequences of our initial assumptions, such as the ratio of the [OIII] lines. The weak predicted strength of the $2.058\mu\text{m}$ line can be explained by the $\text{HeI } 2^3\text{S}$ level being predominantly depopulated by collisions to the singlet levels and not photoionisation, as the model of Clegg & Harrington (1989) also shows. In addition, the predicted strength of the $2.058\mu\text{m}$ is highly dependent on both the dust to gas ratio and on the nature of the dust grains present. Since these factors have only a relatively weak impact on the other lines we have considered it is possible that some of the difference be-

tween the model and the observations may also lie here. For the discrepancies with the low ionisation species observed, both [SII] and [FeII] can exist in extended partially ionised regions which were not explicitly allowed for in the model, and therefore they can only be stronger than the model predicts. The failure to find a good match to the data when we place a low density region near the exciting stars (and hence why we cannot reproduce the [OIII] ratios) probably indicates that spherical symmetry is a poor assumption as noted by Colgan et al. The major concern is that we cannot achieve a good fit to the neon lines. Higher stellar effective temperatures would result in lower predicted [NeII] flux, but the [SIV] flux would then be too large. Colgan et al. find a somewhat similar problem in their model, since when they scale the neon abundance to make the [NeII] line fit, the [NeIII] lines are discrepant. We are confident however that the generally good agreement with the model for most species indicates that the correct model for the stellar population of G45.12+0.13 is that with a cutoff at both low and high masses such that there are no stars less massive than $\sim 20 M_{\odot}$ or more massive than $\sim 50 M_{\odot}$.

Lastly, we note that Hoare et al. (1991) carried out a similar modelling process for the mid-IR lines alone. They quote results only for two pairs of lines ($10.5\mu\text{m}$ [SIV]/ $18.7\mu\text{m}$ [SIII] and $15.4\mu\text{m}$ [NeIII]/ $12.8\mu\text{m}$ [NeII]). Only one of their calculations (that using Kurucz atmospheres to model a cluster of stars) is similar to ours. However, they do not obtain a good match to the observed data from their model (they predict ratios of 2.6 and 4.6 respectively). For the same pairs of lines we predict ratios of 1.0 and 1.4 respectively. As noted before the neon lines are a poor fit to the observed data, but our predictions for both pairs are in considerably better agreement with the observed data than those of Hoare et al. The major difference in the assumptions between the models is the density distribution. Hoare et al. assumed a constant (and relatively low) density. This largely explains the difference since the lower density allows the higher energy photons to penetrate to a larger depth, creating larger volumes of high excitation states for all ions.

7 CONCLUSIONS

We have presented high signal to noise spectral data covering $0.9\text{--}2.5\mu\text{m}$ for the compact HII region G45.12+0.13. All of the lines detected by us can be explained by normal recombination and collisional excitation processes. There is no evidence for hot shocked gas (eg. Van Buren et al. 1990) indicative of the bow-shock model, nor for the presence of CO emission features that may have indicated the presence of a remnant accretion disk (Hollenbach et al. 1993).

We used the HI lines present in our data to estimate the near-infrared extinction law in this source and found a dependence on wavelength that is somewhat steeper than normally observed. After accounting for this extinction we were able to show that our data are also consistent with a dense core, with $n_e > 10^4 \text{cm}^{-3}$. This value is considerably larger than previous infrared studies (eg. Colgan et al. 1991) have found. Most of the emission arises from within the central $3'' \times 3''$ region, though our Br γ image reveals considerable extent to the HII region that was not evident from the ra-

dio continuum map of Wood & Churchwell (1989). There is tentative evidence that the higher ionisation species in our data trace higher electron densities, typical of a core-halo model for the HII region.

Using an approximation to the true radiative transfer problem, we showed how the observed HeI triplet lines indicated considerable opacity in the HeI $n^3\text{P--}2^3\text{S}$ series, consistent with the high derived electron density. After consideration of all the possible effects we showed that helium must be fully ionised within the HII region, and that we could set both upper and lower limits to the maximum stellar effective temperature of 38000K and 42000K respectively. We show how these limits can be set independently of a full modelling process, and hope more effort will be put into determining the accuracy of this method theoretically.

Lastly, from a full photoionisation model, we showed that we can model most of the observed data on G45.13+0.12 with an OB star cluster which has a restricted range of stellar masses present. In particular, a model where the upper mass cut-off is set to $50 M_{\odot}$ and the lower mass cut-off to $20 M_{\odot}$ gives a reasonable fit to the emission line spectrum with the general exception of the neon lines. We agree with Colgan et al. that the asymmetry evident in the source will probably explain the other differences we found between the (spherically symmetric) model and the data.

ACKNOWLEDGEMENTS

We would like to thank Melvin Hoare for many useful discussions on HII regions, Derck Smits for providing a machine readable copy of his HeI data and Ruth Doherty for providing the correction coefficients for the $2.058\mu\text{m}$ HeI line. Part of this work was carried out whilst SLL was supported by an SERC postdoctoral fellowship at the University of Oxford. SLL would also like to thank ANSTO for their financial support during some of these observations.

REFERENCES

- Allen D.A., Barton, J.R., Burton, M.G., Davies, H., Farrell, T.J., Gillingham, P.R., Lankshear, A.F., Lindner, P.L., Mayfield, D.J., Meadows, V.S., Schafer, G.E., Shortridge, K.E.A., 1993, PASA, 10, 298
- Berrington, K.A., Zeippen, C.J., Le Dourneuf, M., Eissner, W., Burke, P.G., 1991, J.Phys.B:At.Mol.Opt.Phys., 24, 3467
- Brown, R.L., Mathews, W.G., 1970, ApJ, 160, 939
- Carpenter, J.M., Snell, R.L., Schloerb, F.P., Skrutskie, M.F., 1993, ApJ, 407, 657
- Cesaroni R., Walmsley C.M., Kömpe C., Churchwell E., 1991, A&A, 252, 278
- Churchwell, E., Walmsley, C.M., Wood, D.O.S., Steppe, H., 1990, Radio Recombination Lines: 25 Years of Investigation, p. 73
- Churchwell, E., Walmsley, C.M., Wood, D.O.S., 1990, A&AS, 83, 119
- Clegg, R.E.S., 1987, MNRAS, 229, 31P
- Clegg, R.E.S., Harrington, J.P., 1989, MNRAS, 239, 869
- Colgan, S.W.J., Simpson, J.P., Rubin, R.H., Erickson, E.F., Haas, M.R., Wolf, J., 1991, ApJ, 366, 172

- Doherty, R.M., Puxley, P.J., Doyon, R., Brand, P.W.J.L., 1994, MNRAS, 266, 497
- Doherty, R.M., Puxley, P.J., Lumsden, S.L., Doyon, R., 1995, MNRAS, in press
- Doyon, R., Puxley, P.J., Joseph, R.D., 1992, ApJ, 397, 117
- Dyson, J.E., Williams, R.J.R., Redman, M.P., 1996, MNRAS, in press
- Ferland, G.J., 1980, PASP, 92, 596
- Ferland, G.J., 1993, University of Kentucky, Department of Physics and Astronomy Internal Report
- Garay, G., Reid, M.J., Moran, J.M., 1985, ApJ, 289, 681
- Garstang, R.H., 1957, MNRAS, 117, 393
- Geballe, T.R., Burton, M.G., Isaacman, R., 1991, MNRAS, 253, 75
- Grandi, S.A., 1980, ApJ, 238, 10
- Habing, H.J., Israel, F.P., 1979, ARA&A, 17, 345
- Hamann, F., DePoy, D.L., Johansson, S., Elias, J., 1994, ApJ, 422, 626
- Hefele, H., Wacker, W., Weinberger, R., 1977, A&A, 56, 407
- Herter T., Helfer H.L., Pipher J.L., Forrest W.J., McCarthy J., Houck J.R., Willner S.P., Puetter R.C., Rudy R.J., 1981, ApJ, 250, 186
- Hoare, M.G., Roche, P.F., Glencross, W.N., 1991, MNRAS, 251, 584
- Hollenbach, D., Johnstone, D., Shu, F., ApJ, 428, 654
- Hummer, D.G., Storey, P.J., 1987, MNRAS, 224, 801
- Johansson, S., 1978, Physica Scripta, 18, 217
- Keto, E.R., Ho, P.T.P., Haschick, A.D., 1987, ApJ, 318, 712
- Kurucz, R.L., 1979, ApJS, 40, 1
- Landini, M., Natta, A., Oliva, E., Salinari, P., Moorwood, A.F.M., 1984, A&A, 134, 284
- Lester, D.F., 1979, Ph.D. Thesis, University of California, Santa Cruz
- Lumsden, S.L., Hoare, M.G., 1995, ApJ, in press, to appear Jun 20
- Lumsden, S.L., Puxley, P.J., Doherty, R.M., 1994, MNRAS, 268, 821
- Matthews, H.E., Goss, W.M., Winnberg, A., Habing, H.J., 1977, A&A, 61, 261
- Mendoza, C., 1983, in IAU Symposium 105, Planetary Nebulae, ed. D.R. Flower, Reidel, Dordrecht, p143
- Mountain, C.M., Robertson, D.J., Lee, T.J., Wade, R., 1990, in Crawford, D.L., ed., Instrumentation in Astronomy VII, Proc. SPIE, 1235, 25
- Natta, A., Panagia, N., 1984, ApJ, 287, 228
- Nussbaumer, H., Storey, P.J., 1988, A&A, 193, 327
- Oliva, E., Moorwood, A.F.M., Danziger, I.J., 1989, A&A, 214, 307
- Osterbrock, D.E., 1989, Astrophysics of Gaseous Nebulae and AGN, University Science Books, Mill Valley, USA
- Pradhan, A.K., Zhang, H.L., 1993, ApJ, 409, L77
- Puxley, P.J., 1988, PhD thesis, University of Edinburgh
- Robbins, R.R., 1968, ApJ, 151, 511
- Rayner, J., Hodapp, K., Zinnecker, H., 1991, in Astrophysics with Infrared Arrays, ASP Conference Series, Vol 14, p264
- Rubin, R.H., 1968, ApJ, 154, 391
- Rudy, R.J., Erwin, P., Rossano, G.S., Puetter, R.C., 1992, ApJ, 384, 536
- Sawey, P.M.J., Berrington, K.A., 1993, At. Data & Nuc. Data Tables, 55, 81
- Scalo, J.M., 1986, Fund. Cosm. Phys., 11, 1
- Shields, J.C., 1993, ApJ, 419, 181
- Simpson, J.P., Rubin, R.H., 1984, ApJ, 281, 184
- Simpson, J.P., Rubin, R.H., 1990, ApJ, 354, 165
- Smits, D.P., 1991a, MNRAS, 248, 193
- Smits, D.P., 1991b, MNRAS, 251, 316
- Sternberg, A., Dalgarno, A., 1989, ApJ, 338, 197
- Tanaka, M., Yamashita, T., Sato, S., Nislud, M., 1983, PASP, 97, 1112
- Van Buren, D., MacLow, M.-M., Wood, D.O.S., Churchwell, E., 1990, ApJ, 353, 570
- Wink, J.E., Altenhoff, W.J., Mezger, P.G., 1982, A&A, 108, 227
- Wood, D.O.S., Churchwell, E., 1989, ApJS, 69, 831
- Wood, D.O.S., Churchwell, E., Salter, C.J., 1988, ApJ, 325, 694
- Wood, D.O.S., Handa, T., Fukui, Y., Churchwell, E., Sofu, Y., Iwata, T., 1988, ApJ, 326, 884

Date	Wavelength (μm)	Resolution (R)	Integration Time (s)	Airmass
1991 October 24	1–1.2	340	1600	1.64
1991 October 25	1.2–1.4	340	1280	1.14
1991 October 25	1.4–1.6	470	960	1.59
1992 November 15	2–2.4	340	320	1.80
1993 April 4	1.6–1.8	530	960	1.53
1993 April 4	1.7–2.1	340	960	1.25
1993 April 4	2.3–2.5	700	640	1.04

Table 1. Details of the UKIRT Observations.

Date	Wavelength (μm)	Resolution (R)	Integration Time (s)	Airmass
1993 September 23	0.86–1.5	420	1800	1.36
1993 September 23	1.4–2.5	420	600	1.35

Table 2. Details of the AAT Observations.

λ_{obs} (μm)	$\delta\lambda$ (μm) ($\times 10^4$)	Line I.D.	λ_{line} (μm)	Corrected line strength	
				CGS4	IRIS
0.9075	2	[SIII] $^1\text{D}_2 - ^3\text{P}_1$	0.9072		467 ± 29
0.9537	2	[SIII] $^1\text{D}_2 - ^3\text{P}_2$	0.9535		1160 ± 120
1.0052	3	Pa δ	1.0052	43 ± 3	37 ± 6
1.0298 <i>bl</i>	9	[SII] $^2\text{P}_{3/2} - ^2\text{D}_{3/2}$	1.0289	3.0 ± 1.0	
1.0332 <i>bl</i>	9	[SII] $^2\text{P}_{3/2} - ^2\text{D}_{5/2}$	1.0323	6.0 ± 0.8	
1.0348 <i>bl</i>	9	[SII] $^2\text{P}_{1/2} - ^2\text{D}_{3/2}$	1.0339	3.2 ± 1.7	
1.0382 <i>bl</i>	9	[SII] $^2\text{P}_{1/2} - ^2\text{D}_{5/2}$	1.0373	1.2 ± 0.5	
1.0837	3	HeI, $2^3\text{P} - 2^3\text{S}$	1.0833	495 ± 19	497 ± 11
1.0944	3	Pa γ	1.0941	64 ± 2	63 ± 2
1.1296	3	OI, $3^3\text{D}_0 - 3^3\text{P}$	1.1289	1.0 ± 0.2	
1.1887	3	[FeII] $\text{a}^2\text{G}_{7/2} - \text{a}^4\text{D}_{7/2}?$	1.1885	0.7 ± 0.1	
1.1973	3	HeI, $5^3\text{D} - 3^3\text{P}$	1.1972	1.6 ± 0.2	1.2 ± 0.1
1.2534	3	HeI, $4^3\text{P} - 3^3\text{S}$	1.2531	2.9 ± 0.1	2.7 ± 0.1
1.2574	3	[FeII] $\text{a}^4\text{D}_{7/2} - \text{a}^6\text{D}_{9/2}$	1.2570	1.7 ± 0.1	1.1 ± 0.1
1.2800 <i>bl</i>	3	HeI, $5^3\text{F} - 3^3\text{D}$	1.2789	$11.3 \pm 0.5\text{bl}$	$6.9 \pm 0.8\text{bl}$
1.2800 <i>bl</i>	3	HeI, $5^1\text{F} - 3^3\text{D}$	1.2794	$11.3 \pm 0.5\text{bl}$	$6.9 \pm 0.8\text{bl}$
1.2827	3	Pa β	1.2821	100 ± 4	100 ± 2
1.2941 <i>bl</i>	4	[FeII] $\text{a}^4\text{D}_{5/2} - \text{a}^6\text{D}_{5/2}$	1.2946	$0.4 \pm 0.1\text{bl}$	
1.2980 <i>bl</i>	4	[FeII] $\text{a}^4\text{D}_{3/2} - \text{a}^6\text{D}_{1/2}$	1.2981	$0.4 \pm 0.1\text{bl}$	
1.2984 <i>bl</i>	4	HeI, $5^3\text{P} - 3^3\text{D}$	1.2988	1.1 ± 0.1	0.9 ± 0.2
1.3171 <i>bl</i>	4	OI, $4^3\text{S}_0 - 3^3\text{P}$	1.3168	2.1 ± 0.1	1.5 ± 0.2
1.3213 <i>bl</i>	3	[FeII] $\text{a}^4\text{D}_{7/2} - \text{a}^6\text{D}_{7/2}$	1.3209	0.4 ± 0.1	0.3 ± 0.1
1.3724	6	[FeII] $\text{a}^4\text{D}_{7/2} - \text{a}^6\text{D}_{5/2}$	1.3722	0.3 ± 0.1	
1.5086 <i>bl</i>	5	Br22–4	1.5087	$1.2 \pm 0.1\text{bl}$	
1.5086 <i>bl</i>	5	HeI, $4^1\text{P} - 3^1\text{S}$	1.5088	$1.2 \pm 0.1\text{bl}$	
1.5138	3	Br21–4	1.5137	0.9 ± 0.1	
1.5196	3	Br20–4	1.5196	1.0 ± 0.1	
1.5266	3	Br19–4	1.5265	0.9 ± 0.1	
1.5345 <i>bl</i>	5	Br18–4	1.5346	$1.5 \pm 0.1\text{bl}$	$1.2 \pm 0.2\text{bl}$
1.5345 <i>bl</i>	5	[FeII] $\text{a}^4\text{D}_{5/2} - \text{a}^4\text{F}_{9/2}$	1.5339	$1.5 \pm 0.1\text{bl}$	$1.2 \pm 0.2\text{bl}$
1.5444	3	Br17–4	1.5443	1.5 ± 0.1	1.2 ± 0.1
1.5562	3	Br16–4	1.5561	1.8 ± 0.1	1.6 ± 0.1
1.5708	3	Br15–4	1.5705	2.1 ± 0.1	1.6 ± 0.1
1.5888	3	Br14–4	1.5885	2.6 ± 0.2	2.3 ± 0.1
1.6005	3	[FeII] $\text{a}^4\text{D}_{3/2} - \text{a}^4\text{F}_{7/2}?$	1.5999	0.2 ± 0.1	
1.6117	3	Br13–4	1.6114	2.7 ± 0.1	2.8 ± 0.1
1.6414 <i>bl</i>	4	Br12–4	1.6412	3.9 ± 0.2	4.2 ± 0.1
1.6444 <i>bl</i>	4	[FeII] $\text{a}^4\text{D}_{7/2} - \text{a}^4\text{F}_{9/2}$	1.6440	3.9 ± 0.2	4.2 ± 0.1
1.6640	5	[FeII] $\text{a}^4\text{D}_{1/2} - \text{a}^4\text{F}_{5/2}$	1.6642	0.10 ± 0.07	
1.6776	3	[FeII] $\text{a}^4\text{D}_{5/2} - \text{a}^4\text{F}_{7/2}$	1.6773	0.3 ± 0.1	
1.6812	3	Br11–4	1.6811	4.4 ± 0.2	4.9 ± 0.2

Table 3. Identifications of detected lines. Identifications which are unsure are marked with a ?. The Pa β flux after correction for extinction is $1.64 \times 10^{-13} \text{Wm}^{-2}$ (CGS4) and $9.83 \times 10^{-14} \text{Wm}^{-2}$ (IRIS). All strengths are quoted relative to $F(\text{Pa}\beta) = 100$.

λ_{obs} (μm)	$\delta\lambda$ (μm) ($\times 10^4$)	Line I.D.	λ_{line} (μm)	Corrected line strength	
				CGS4	IRIS
1.7011	3	HeI, $4^3\text{D}-3^3\text{P}$	1.7007	2.1 ± 0.1	2.5 ± 0.1
1.7370	3	Br10-4	1.7367	6.3 ± 0.2	6.8 ± 0.1
1.7456 <i>bl</i>	3	[FeII] $\text{a}^4\text{D}_{1/2}-\text{a}^4\text{F}_{3/2}$	1.7454	$0.3 \pm 0.1\text{bl}$	$0.4 \pm 0.1\text{bl}$
1.7456 <i>bl</i>	3	HeI, $7^3\text{P}-4^3\text{S}$	1.7455	$0.3 \pm 0.1\text{bl}$	$0.4 \pm 0.1\text{bl}$
1.7978 <i>bl</i>	3	[FeII] $\text{a}^4\text{D}_{3/2}-\text{a}^4\text{F}_{3/2}$?	1.7976	$0.2 \pm 0.1\text{bl}$	
1.8008 <i>bl</i>	3	[FeII] $\text{a}^4\text{D}_{5/2}-\text{a}^4\text{F}_{5/2}$?	1.8005	$0.3 \pm 0.1\text{bl}$	
1.8178	5	Br9-4	1.8179	11.4 ± 0.4	6.0 ± 0.1
1.8746	7	Pa α	1.8756	305 ± 12	
1.9093	5	HeI, $4^1\text{D}-3^1\text{P}$	1.9095	1.2 ± 0.1	
1.9449	5	Br δ	1.9451	14.5 ± 0.6	14.2 ± 0.1
1.9547	5	HeI, $4^3\text{P}-3^3\text{D}$	1.9549	2.1 ± 0.1	1.3 ± 0.1
2.0583	5	HeI, $2^1\text{P}-2^1\text{S}$	2.0587	23.2 ± 0.9	19.2 ± 0.2
2.1128 <i>bl</i>	5	HeI, $4^3\text{S}-3^3\text{P}$	2.1126	$1.0 \pm 0.1\text{bl}$	$1.1 \pm 0.1\text{bl}$
2.1128 <i>bl</i>	5	HeI, $4^1\text{S}-3^1\text{P}$	2.1138	$1.0 \pm 0.1\text{bl}$	$1.1 \pm 0.1\text{bl}$
2.1210 <i>bl</i> ?	5	H ₂ , $2-1\text{S}(0)$	2.1218	$0.09 \pm 0.06\text{bl}$	
2.1460	5	[FeIII] $\text{a}^3\text{G}_3-\text{a}^3\text{H}_4$?	2.1457	0.16 ± 0.05	0.18 ± 0.05
2.1657	5	Br γ	2.1661	19.0 ± 1.0	18.5 ± 0.1
2.2185	5	[FeIII] $\text{a}^3\text{G}_5-\text{a}^3\text{H}_6$	2.2183	0.42 ± 0.05	0.28 ± 0.05
2.2418	5	[FeIII] $\text{a}^3\text{G}_4-\text{a}^3\text{H}_4$?	2.2427	0.21 ± 0.05	0.16 ± 0.05
2.2854	5	?		0.27 ± 0.06	0.22 ± 0.05
2.3487 <i>bl</i>	3	[FeIII] $\text{a}^3\text{G}_5-\text{a}^3\text{H}_5$	2.3485	$0.44 \pm 0.06\text{bl}$	
2.3487 <i>bl</i>	3	Pf29-5	2.3492	$0.44 \pm 0.06\text{bl}$	
2.3662	3	Pf26-5	2.3669	0.28 ± 0.10	
2.3737	3	Pf25-5	2.3744	0.28 ± 0.08	
2.3824	3	Pf24-5	2.3828	0.32 ± 0.10	
2.3919	3	Pf23-5	2.3925	0.33 ± 0.06	
2.4033 <i>bl</i>	3	Pf22-5	2.4036	$0.40 \pm 0.07\text{bl}$	
2.4063 <i>bl</i>	5	H ₂ , $1-0 \text{ Q}_1$	2.4066	$0.16 \pm 0.07\text{bl}$	
2.4155	3	Pf21-5	2.4164	0.66 ± 0.31	
2.4310	3	Pf20-5	2.4314	0.43 ± 0.10	
2.4486	3	Pf19-5	2.4490	0.73 ± 0.11	
2.4693	3	Pf18-5	2.4700	0.74 ± 0.11	
2.4942	3	Pf17-5	2.4953	0.87 ± 0.15	

Table 3. Identifications of detected lines. Identifications which are unsure are marked with a ?. All strengths are quoted relative to $F(\text{Pa}\beta) = 100$.

Line ID	$\lambda(\mu\text{m})$	Observed Ratio	Theoretical Ratio (Smits)	
			$T_e = 5000\text{K}$	$T_e = 10000\text{K}$
$2^3\text{P}-2^3\text{S}$	1.083	235 ± 14	165	450
$5^3\text{D}-3^3\text{P}$	1.198	0.76 ± 0.10	0.67	0.70
$4^3\text{P}-3^3\text{S}$	1.253	1.38 ± 0.08	0.33	0.41
$5^{1,3}\text{F}-3^{1,3}\text{D}$	1.279 <i>bl</i>	5.4 ± 2.0	3.4	3.0
$5^3\text{P}-3^3\text{D}$	1.298 <i>bl</i>	0.52 ± 0.05	0.11	0.13
$4^1\text{P}-3^1\text{S}$	1.508 <i>bl</i>	0.19 ± 0.05	0.15	0.17
$7^3\text{P}-4^3\text{S}$	1.745 <i>bl</i>	0.16 ± 0.06	0.02	0.03
$4^1\text{D}-3^1\text{P}$	1.909	0.57 ± 0.05	0.36	0.35
$4^3\text{P}-3^3\text{D}$	1.955	1.00 ± 0.06	0.21	0.26
$2^1\text{P}-2^1\text{S}$	2.058	11.0 ± 0.7	10.9	15.6
$4^{1,3}\text{S}-3^{1,3}\text{P}$	2.113 <i>bl</i>	0.48 ± 0.05	0.24	0.33

Table 4. Observed and predicted HeI line ratios against the $1.7007\mu\text{m}$ $4^3\text{D}-3^3\text{P}$ transition. Theoretical values are given for $T_e = 5000\text{K}$ and 10000K , and are independent of density, with the exception of the $2\text{P}-2\text{S}$ lines. These are quoted for $n_e = 10^4\text{cm}^{-3}$, and are also further discussed in the text since they are affected by processes not included in Smits theoretical data. The observed values come from the CGS4 data. A *bl* after the wavelength indicates a line that is completely blended with another feature: the strength of the line has been derived as indicated in the text. Only those lines blended with HI features are likely to have completely accurate line strengths quoted.

Line	$\lambda(\mu\text{m})$	Observed Ratio	Theoretical Ratio	n_e (cm^{-3})
$a^4D_{5/2}-a^6D_{5/2}$	1.294	0.24 ± 0.06	0.02–0.25	10000^{+30000}_{-6000}
$a^4D_{3/2}-a^6D_{1/2}$	1.298	0.24 ± 0.06	0.003–0.08	10000^{+30000}_{-6000}
$a^4D_{7/2}-a^6D_{7/2}$	1.321	0.24 ± 0.06	0.262	
$a^4D_{7/2}-a^6D_{5/2}$	1.372	0.16 ± 0.06	0.171	
$a^4D_{3/2}-a^4F_{7/2}$	1.601	0.14 ± 0.05	0.008–0.2	15000^{+35000}_{-8000}
$a^4D_{7/2}-a^4F_{9/2}$	1.644	0.67 ± 0.05	0.74	
$a^4D_{1/2}-a^4F_{5/2}$	1.664	0.06 ± 0.05	0.003–0.12	10000^{+50000}_{-9000}
$a^4D_{5/2}-a^4F_{7/2}$	1.677	0.18 ± 0.06	0.01–0.2	$30000^{+\infty}_{-20000}$
$a^4D_{1/2}-a^4F_{3/2}$	1.745	0.20 ± 0.04	0.002–0.06	
$a^4D_{3/2}-a^4F_{3/2}$	1.798	0.12 ± 0.06	0.004–0.1	> 15000
$a^4D_{5/2}-a^4F_{5/2}$	1.801	0.18 ± 0.06	0.009–0.14	> 15000

Table 5. Observed and predicted [FeII] line ratios against the $1.257\mu\text{m } a^6D_{9/2}-a^4D_{7/2}$ transition. Theoretical values assume $T_e = 7500\text{K}$ and span the density range $10-10^6\text{cm}^{-3}$. Where only one value is given, this transition shares a common upper level with the $1.257\mu\text{m}$ line. The pair of lines at $1.294/1.298\mu\text{m}$ are blended, so we have used the sum of the theoretical data to match the observed value.

Line	$\lambda(\mu\text{m})$	Observed Flux (10^{-14} Wm^{-2})	Dereddened Flux	Observed Ratio with Pa β	Model Ratio with Pa β
[SIII]	0.953			11.6 ± 1.2	10.0
[SII]	1.03			0.13 ± 0.02	0.05
HeI	1.083			5.0 ± 0.2	4.2
[FeII]	1.257			> 0.03	0.007
HeI	1.701			0.02 ± 0.001	0.02
HeI	2.058			0.2 ± 0.01	0.06
[ArII]	6.99	< 7.8	< 13.5	< 0.55	0.02
[ArIII]	8.99	3.3 ± 0.4	20 ± 2	0.8 ± 0.1	1.1
[SIV]	10.5	< 12	< 80	< 3.4	1.5
[NeII]	12.8	26 ± 2.6	52 ± 5	2.2 ± 0.3	3.4
[NeIII]	15.4	< 19	< 36	< 1.5	4.6
[SIII]	18.7	15.8 ± 1.9	38 ± 5	1.5 ± 0.2	1.5
[SIII]	33.5	7.4 ± 0.7	10.0 ± 1.0	0.42 ± 0.05	0.20
[NeIII]	36.0	5.0 ± 0.7	6.4 ± 0.8	0.26 ± 0.03	0.23
[OIII]	51.8	17.4 ± 1.3	20 ± 1.5	0.84 ± 0.06	1.0
[NIII]	57.3	3.6 ± 0.7	4.0 ± 0.8	0.16 ± 0.03	0.13
[OIII]	88.4	4.6 ± 0.3	5.0 ± 0.5	0.21 ± 0.02	0.11

Table 6. Adopted mid and far-IR line fluxes from the literature. Sources are given in the text. The extinction correction applied follows that of Colgan et al. The near-IR values are taken from Table 3, and only the ratio with Pa β is repeated here. The values for the [FeII] and [SII] lines are summed over the relevant multiplets to match the output from Cloudy. Since not all the [FeII] lines were observed, a lower limit is given by summing all those observed. The model ratios are for the best fitting photoionisation model as described in the text.

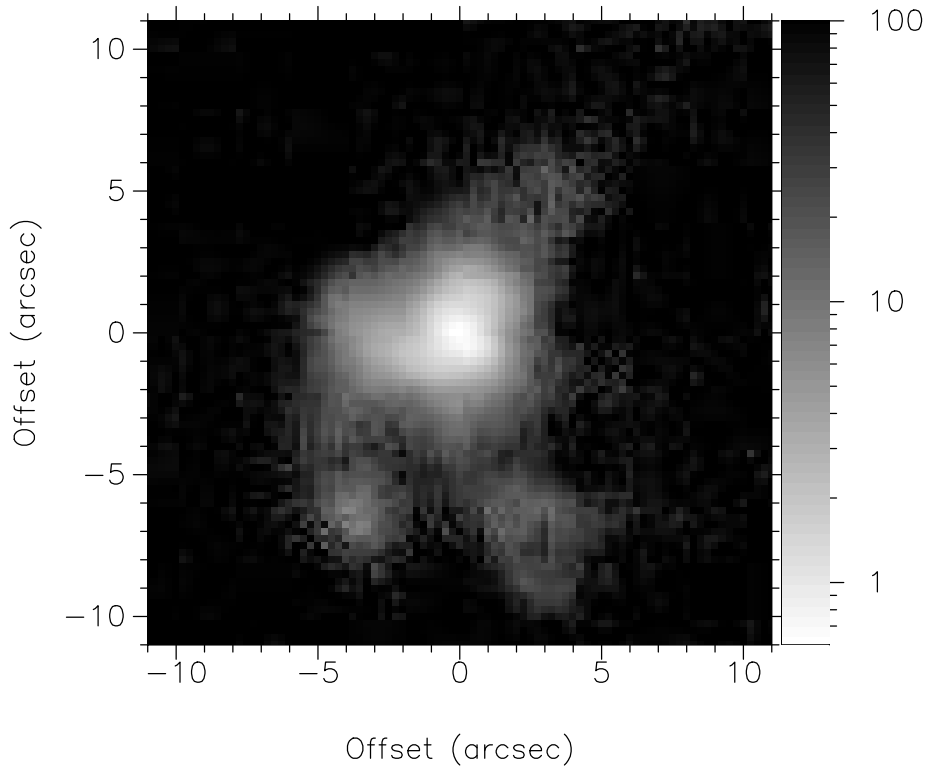


Figure 1: Greyscale $\text{Br}\gamma$ image of G45.12+0.13. The log of the observed intensity is plotted. No absolute calibration is given due to the non-photometric conditions during these observations. The (0,0) position is assumed to correspond to the peak in the 2cm radio map. Extended emission not evident in the radio map (figure 23a of Wood & Churchwell 1989) is obvious in our map.

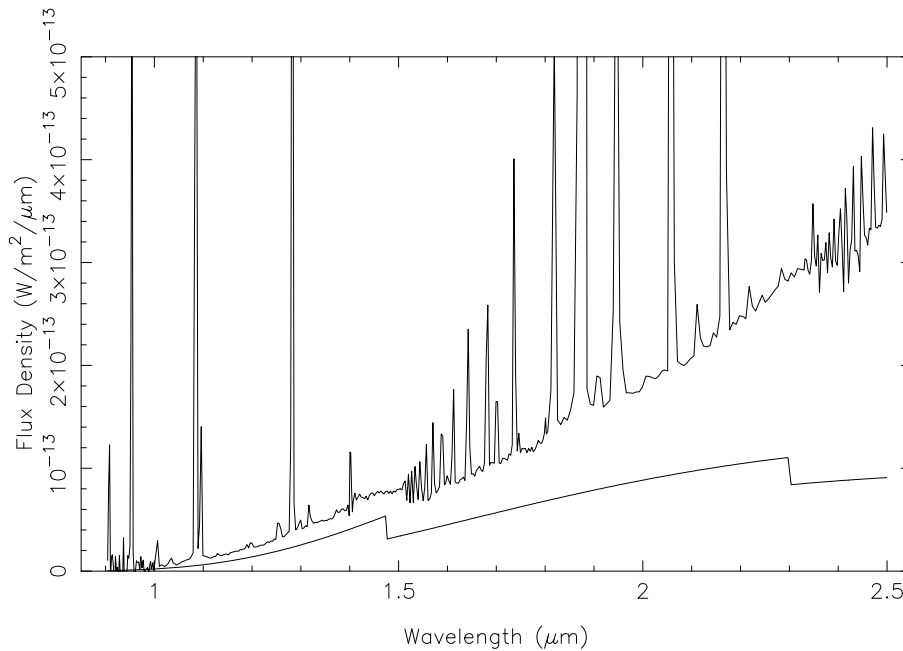


Figure 2: Observed spectrum of G45.12+0.13 with the stronger lines suppressed to show the weaker features present. The solid line at the bottom is the 'best' match to the expected free-free component (scaled to the observed $\text{Pa}\beta$ line strength) as described in section 5.6, including the correct allowance for the observed extinction.

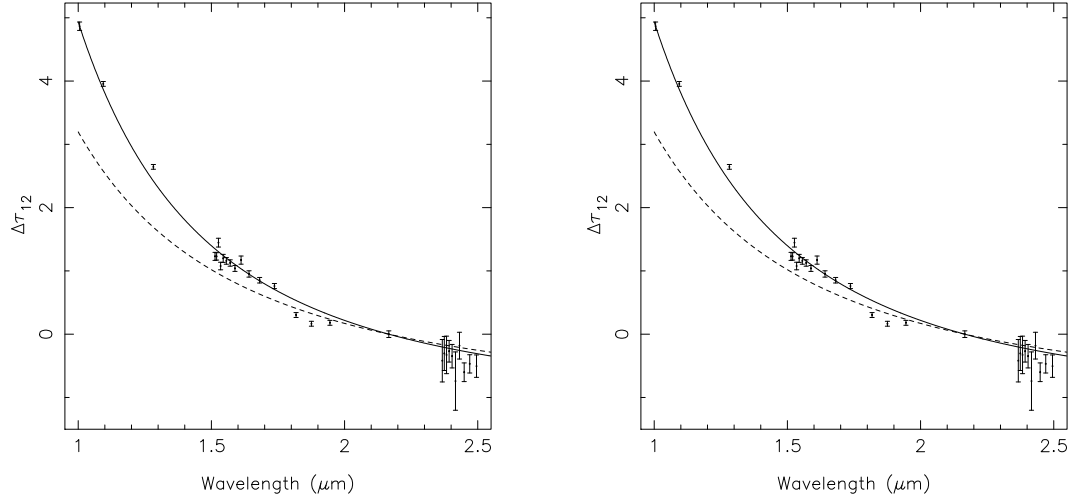


Figure 3: Observed values of the extinction for (a) the CGS4 data and (b) the IRIS data. The derived best fit to α and $\tau_{\text{Br}\gamma}$ is shown as a solid line. The dashed line represents the extinction law given by Landini et al. (1984).

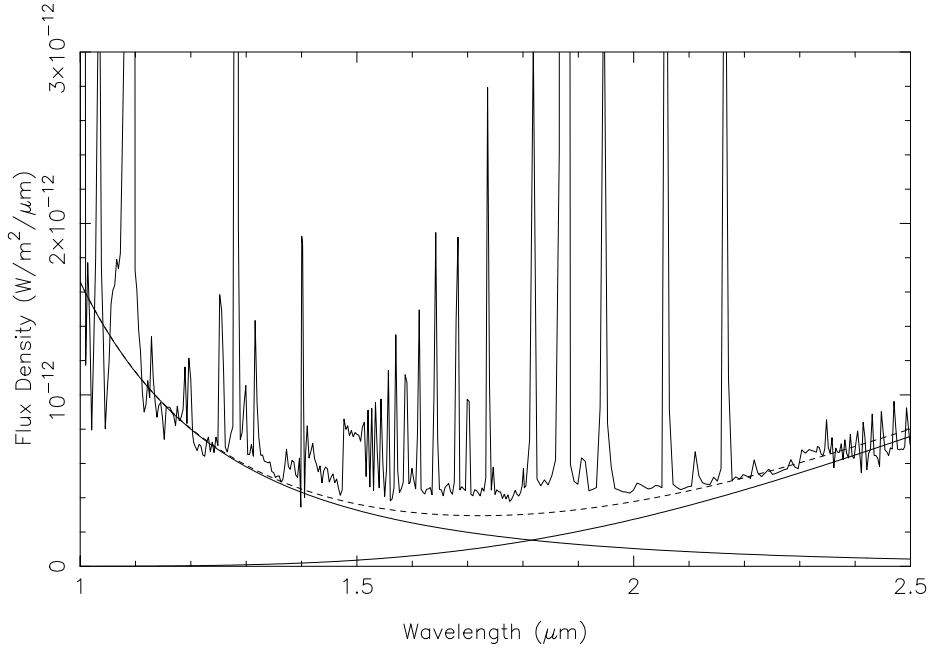


Figure 4: The spectrum of G45.12+0.13 after removing the free-free component shown in figure 2, and after correcting for extinction. The two solid lines represent simple models for (i) starlight (rising to shorter wavelengths) and (ii) dust modified by a grey-body law (rising to longer wavelengths). The dashed line is the sum of these two components and can be seen to be a good match to the residual continuum emission. Note also the prominent blends of emission lines just longwards of the Brackett and Pfund limits mentioned in the text.